6.1 INTRODUCTION

The present chapter investigates the corrosion behavior of additively manufactured (AM) maraging steel built with different build orientations of 0°, 45° and 90°, in comparison with the behavior of conventionally produced maraging steel, in a 3.5% NaCl solution. The effect of build orientation and aging treatment on the corrosion resistance was studied. The results highlight the importance of optimizing build orientation and heat treatment for improving the corrosion resistance of AM maraging steel.

Corrosion behavior was studied using a three-electrode cell and electrochemical experiments were performed using a Potentiostate for AM maraging steel in the orientations of 0°, 45° and 90° and also in heat treated condition. The behaviour was compared with the performance of the conventionally manufactured maraging steel.

6.2 Corrosion Behaviour

6.2.1 Microstructural Characterization

Schematic representation of the three plates, printed in different orientations (0°, 45° and 90°) depicting layers, and the sides exposed during corrosion, is displayed in Fig.6.1.

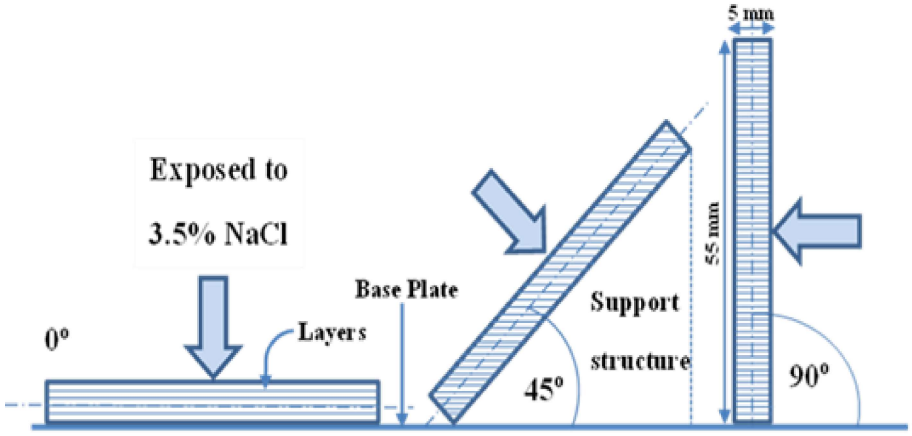

Fig. 6.1 Schematic representation of three plates printed in different orientations, depicting layers, along with the exposer side during corrosion, shown by arrows.

The microstructure of the conventionally manufactured (cast and hot rolled) specimens in as received and HT conditions are shown in Fig.6.2. The conventional specimen in the as-received (CM) condition shows large equiaxed grains of ~50 µm size as given in Fig.6.2(a), and after heat treatment (CM-HT), lath martensite can be seen in Fig. 6.2(b).

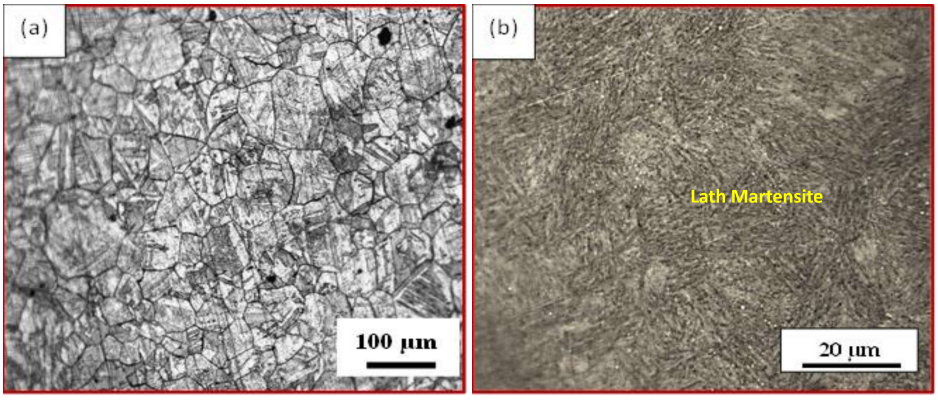

Fig.6.2 Optical micrograph of maraging steel: (a) Coarse microstructure in CM condition and (b) lath martensite in CM-HT condition.

The strip-shaped and arc-shaped melt tracks that arise from the melting route of the laser beam using the "track-by-track" and "layer-by-layer" approaches can be seen clearly in Figs. 6.3(a), 6.4(a) and 6.5(a) respectively. The inset Fig. 6.3(a') shows the top view microstructure at lower magnification which depicts laser hatch and interlayer rotation (i.e. 67°). The inset Fig. 6.4(a'), shows the build layers oriented in 45° depict the inclined elliptical melt pool, similarly, Fig. 6.5(a') depicts the build layers with a shallow melt pool. In the AB, sample, at lower magnification, laser tracks, hatching, melt pool characteristics and build layers can be seen. However, at higher magnifications, cellular and columnar grains of sub-micron size are revealed. In Fig. 6.3(a), the AB specimen in 0° orientation shows laser tracks. In the specimens oriented at 45° and 90°, the area of interest lies towards the side of the build layers, due to which the melt pools of semi-elliptical in shape can be seen in Figs. 6.4(a) and 6.5(a). In all AB specimens, two types

of microstructures, cellular grains (0.2µm -1µm size) and columnar grains with a length of ~20µm and width of ~0.5µm can be observed. In Figs. 6.3(b), 6.4(b) and 6.5(b), partially diffused laser tracks and melt-pool characteristics can be observed and fine lath martensitic microstructure can be seen after heat treatment in AM samples.

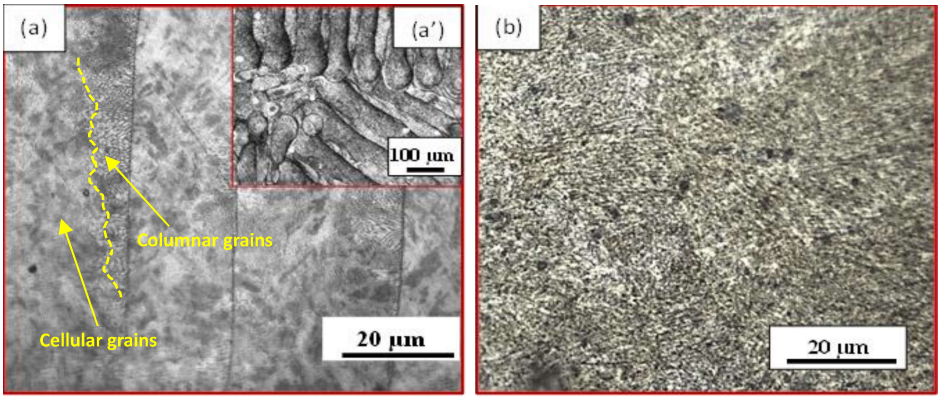

Fig. 6.3 Optical micrograph depicting: (a) laser tracks with fine cellular and columnar structure (a') interlayer rotation in 0° AB condition and (b) very fine martensite with no tracks residue after heat treatment in 0° HT condition.

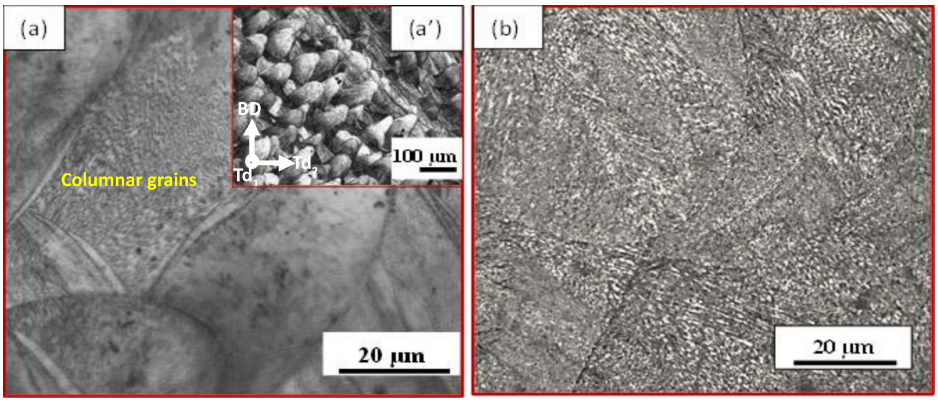

Fig. 6.4 Optical micrographs depicting: (a) very fine microstructure, (a') inclined melt pool in 45° AB condition and (b) martensite with partial melt pool characteristic in 45° HT condition.

Partial processing characteristics still can be seen in AM-HT samples, as the selected solution treatment temperature (815°C) lies in the lower temperature range of austenitization in maraging steels [162].

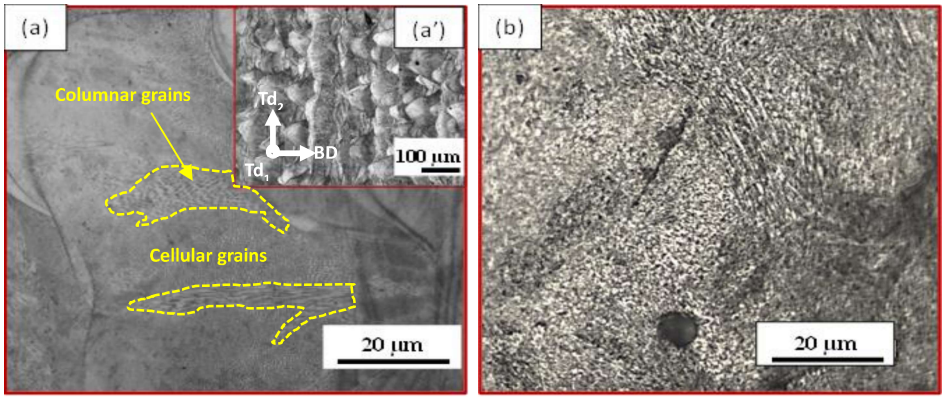

Fig. 6.5 Optical micrographs depicting: (a) semi-elliptical melt pool, (a') series of layers with melt pool in 90° AB condition and (b) fine martensite with partial melt pool characteristics in 90° HT condition.

6.2.2 Open-circuit Potential and Potentiodynamic Polarization

6.2.2.1 In As-Built (AB/AR) Condition

It was observed, that OCP for the 0°, 45° and 90° AB samples, was found to be -0.36±0.05 V, -0.34±0.06 V and -0.34±0.08 V, respectively as given in Table. 6.1 The higher the OCP value, the nobler the material. Low OCP, on the other hand, implies that the material is active [163]. The potentiodynamic results of CM and AB samples are reported in Fig. 6.6(a). The corrosion potential (E_{corr}), corrosion current density (I_{corr}), and corrosion rate (mm/a) of the specimens calculated from Tafel curves are summarized in Table 6.1. E_{corr} : -0.34±0.04 V, I_{corr} : 1.2±0.8 µA/cm^2 and E_{corr} : -0.46±0.04, I_{corr} : 0.89±0.01 µA/cm^2 values are for the 90° and 0° AB samples, respectively. Corrosion current for the 45° AB samples was 0.93±0.03 µA/cm^2, which is lower than that of 90° AB sample and higher than that of the 0° AB samples. Thus, it is seen that I_{corr} value increases as the inclination angle increases. In summary, corrosion current density of the AB sample in 0° AB build direction is 0.89±0.01 µA/cm^2 < 45° AB (I_{corr}: 0.93±0.03 µA/cm^2) < 90° AB (I_{corr}:1.2±0.8 µA/cm^2). The degree of heat transfer is more in 0° AB plates followed by 45° AB and 90° AB plates due to which 0° AB samples showed comparatively finer microstructure

than 45° AB and 90° AB samples. Therefore, 0° AB samples possess maximum grain boundary density followed by 45° AB and 90° AB samples. This might be a reason for observed trends of corrosion rate in AB AM samples. The CM sample showed I_{corr}: 4.87±0.6 μA/cm^2, which is greater than the AB samples. In general, a lower I_{corr} value indicates greater resistance to corrosion and a slower rate of corrosion. These findings indicate that as the build orientation increases from 0° to 90° in the AB condition, the corrosion rate increases.

6.2.2.2 In Heat Treated (HT) Condition

The OCP of the 0°, 45° and 90° HT samples found -0.37±0.02 V, -0.37±0.04 & -0.37±0.05 V, respectively. For the conventional samples in as received and HT conditions, OCP observed -0.33±0.01 V and -0.35±0.04 V, respectively. The potentiodynamic polarization curves of HT specimens are shown in Fig. 6.6(b) and the values of difference are represented in Table 6.1. The corrosion current density of AB HT specimens for different build orientations is measured as: 0° orientation (I_{corr} = 3.91±0.1 μA/cm^2) < 90° orientation (I_{corr} = 9.37±0.7 μA/cm^2) < 45° orientation (I_{corr} = 10.2±0.5 μA/cm^2).

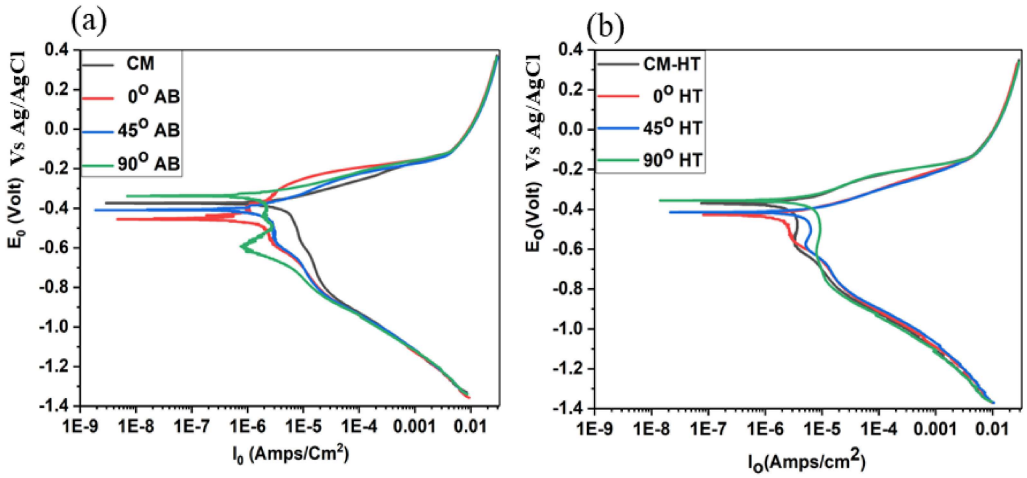

Fig. 6.6 (a) Potentiodynamic polarization curves of CM and AB condition in different orientations (b) Potentiodynamic polarization curves in AM-HT and CM-HT conditions.

This pattern might have been influenced by the amount of reverted austenite generated in the samples following heat treatment. The CM-HT sample showed I_{corr}: 5.23±0.2 μA/cm^2, which is greater than 0^o HT and lower than 45^o and 90^o HT samples. Comparing the I_{corr} values and Figs. 6.6(a) and 6.6(b), it is clear that HT maraging steel exhibited a higher degree of activity than AB additive and CM, as received conventional samples.

Table: 6.1 Electrochemical parameters of maraging steel in different conditions, extracted from polarization plots fitted in the Tafel region.

Samples	OCP (Volt)	I_{corr} (μA/cm^2)	E_{corr} (Volt)	Corrosion Rate (mm/a)
CM	-0.33±0.01	4.87±0.6	-0.37±0.08	0.057±0.005
CM-HT	-0.35±0.04	5.23±0.2	-0.37±0.05	0.061±0.002
0^o AB	-0.36±0.05	0.89±0.01	-0.46±0.04	0.010±0.001
0^o HT	-0.37±0.02	3.92±0.1	-0.43±0.06	0.046±0.004
45^o AB	-0.34±0.06	0.93±0.03	-0.41±0.04	0.011±0.008
45^o HT	-0.37±0.04	10.2±0.5	-0.41±0.07	0.120±0.002
90^o AB	-0.34±0.08	1.21±0.8	-0.34±0.04	0.014±0.004
90^o HT	-0.37±0.05	9.37±0.7	-0.36±0.05	0.109±0.008

6.2.3 Electrochemical Impedance Spectroscopy (EIS)

The impedance spectra for the AB and AM-HT specimens, as well CM and CM-HT conventional specimens, were obtained using Nyquist plots. Fig. 6.7 depicts Nyquist plots for AB additive and as received conventional (CM) specimens, while Fig. 6.8 depicts Nyquist plots for the heat-treated conventional (CM-HT) and heat-treated additive samples. It is obvious that the diameter of the arc decreased with increasing inclination angle from 0^o, 45^o and 90^o in AB samples, implying a decrease in resistance

of charge transfer. Large localized heterogeneity in the interlayer region and higher surface energy of the AB samples with 90° orientation led to lower corrosion resistance.

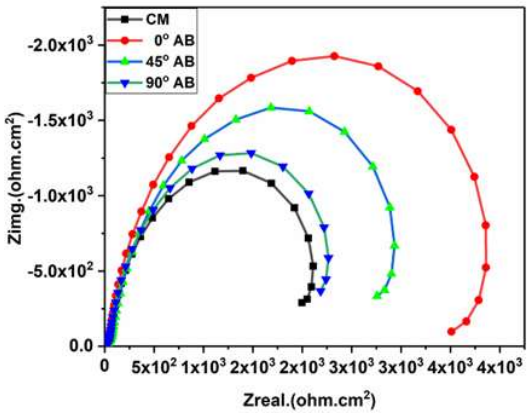

Fig. 6.7. Nyquist plots in the CM and AB conditions.

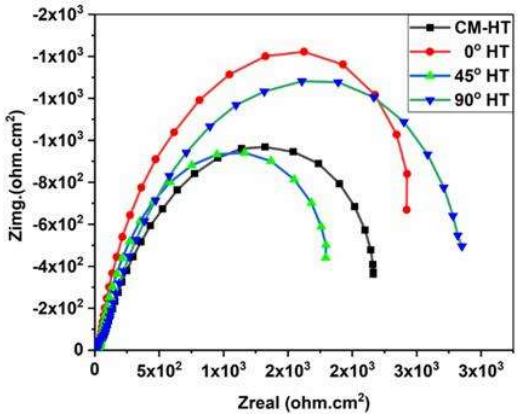

Fig. 6.8 Nyquist plots in CM-HT and AM-HT conditions.

Also, lower corrosion resistance for conventional sample with a coarser microstructure was observed. Therefore, the corrosion resistance of CM and 90° AB were found to be comparable. From the Nyquist plots of the HT samples, it was found that 0° oriented samples had the highest arc diameter, followed by 90° and 45° oriented samples. The arc diameter of CM-HT samples was found to be between 90° HT and 45° HT samples. This pattern might have been influenced by the amount of reverted austenite generated in the samples following solution and aging treatment (HT). Diffused segregation of reverted austenite, forms structural heterogeneity which results in micro-galvanic cell formation

at the interface of the martensite matrix and reverted austenite. There was a combined effect of precipitation of intermetallic phases and reverted austenite, in reducing its corrosion resistance. The lower corrosion resistance of the sample with built orientation of 45° HT condition was due to large extent of reverted austenite in the HT condition. Therefore, the corrosion resistance in these two conditions is comparable. Figs. 6.9(a, b) and 6.10(a, b) illustrate the EIS results using Bode graphs.

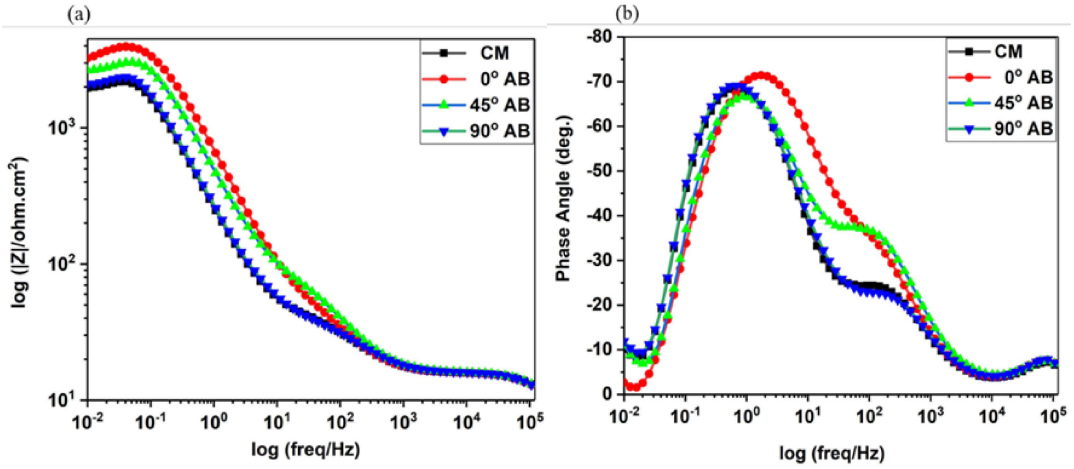

Fig. 6.9. Bode plot of CM and AB specimens in different orientations: (a) log-log plot of |Z| vs. log freq. (b) plot of phase angle vs. log freq.

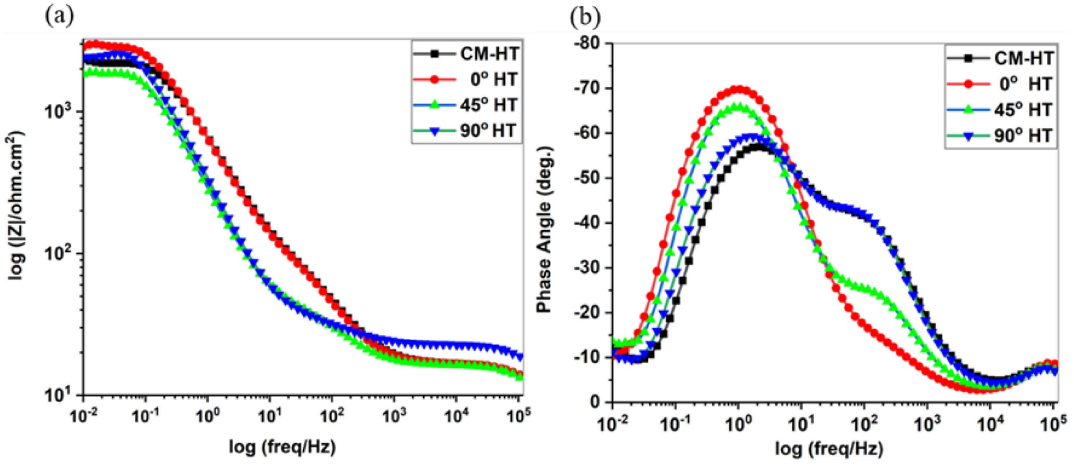

Fig. 6.10. Bode plots of CM-HT and AM-HT specimens: (a) log-log plot of |Z| vs. log freq. (b) plot of phase angle vs. log freq.

These EIS spectra have been fitted to the best equivalent circuit model, R_1, QPE_1, R_2, L_1, R_3, as shown in Fig. 6.11. Table 6.12 shows the EIS parameters determined by fitting the circuit depicted in the relevant figure in various notation forms. According to the universal definition, the circuit's elements are as follows: R_1 denotes solution resistance, QPE_1 denotes constant phase elements, R_2 denotes polarisation resistance, which can be characterized as charge transfer resistance [164], R_3 denotes intermediate layer resistance, and L denotes intermediate layer inductance. There was little contribution of inductance which can be seen in Table 6.2, and the inductive loops were distinctly visible in AM samples. After heat treatment, the effect is minimal as can be seen in Table 6.2. The result shows that the charge transfer resistance decreased with increasing inclination angle in the AB samples. In the HT condition, the 45° HT sample had the lowest charge transfer resistance.

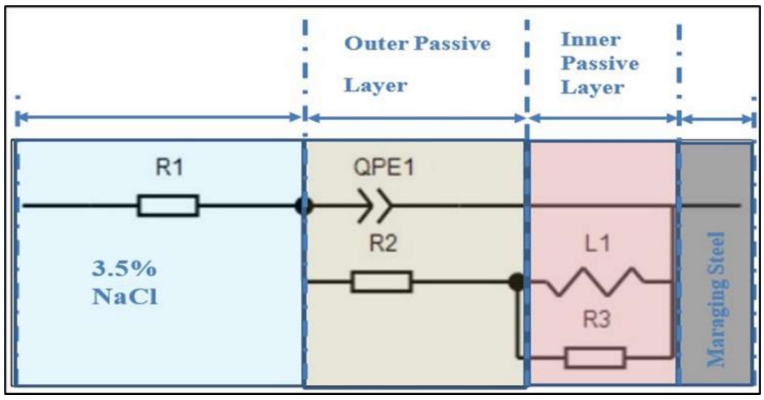

Fig. 6.11. Equivalent circuit diagram of fitting EIS data. In this diagram R1, R2 and R3 represent the solution resistance, charge transfer resistance of outer region of passive film, and inner layer charge transfer resistance. QPE1, L1 is constant phase angle element of outer layer and inductance of inner layer respectively.

Bode charts illustrate the relationship between the impedance modulus, the phase angle, and the frequency. Figs. 6.9(a, b) illustrate the properties of the impedance modulus-frequency relationship. R_1 is represented by the impedance modulus measured in the

highest frequency area of the Log Z-Log f, Bode graphs. In the lowest frequency range, the impedance modulus equals the sum of R_1 and R_2 [165]. There is no discernible difference in solution resistance R_1 for AB/CM and HT samples, which is ~15.7 $\Omega.cm^2$. The total of R_1 and R_2 reduces as the inclination angle increases in the AB samples. Similarly, the 45° oriented HT samples showed the lowest R_1 plus R_2 followed by 90° and 0° HT. R_2 is proportional to the degree of electrochemical reaction in the inverse direction [166]. Fig. 6.8, demonstrates that as the reverted austenite content increases in the 45° HT sample, the charge transfer resistance of the corrosion reaction decreases and the degree of corrosion reaction increases.

The phase angle curves of the AB and AM-HT samples, as well as the conventional sample, are found to be identical. The phase angle reached a maximum value of less than 80° for both AB/CM and HT samples, showing a stable passive layer formed on the surface in solution. The low-frequency portion has a definite peak, while the intermediate and high-frequency portions have a tiny hump. Except for the 0° AB and 0° HT samples, the slight hump in the middle and high-frequency zones is more noticeable. All of this can be seen in Fig. 6.9(b) and Fig. 6.10(b) which imply corrosion is represented by two-time constants. This indicates that two-state factors, the double electric layer and corrosion products, influenced the electrochemical reactivity of the AM and conventional maraging steel specimens [167].

Table 6.2 EIS Data, simulation using CS Studio software for maraging steel in different conditions.

Specimens	R_1 Ω. cm^2	QPE-Q 10^{-5} .F. cm^{-2} s^n	QPE-n N/A	R_2 Ω. cm^2	L_1 H.cm^2	R_3 10^{10}.Ω. cm^2
CM	16.65±0.8	4.17±0.4	0.68±0.01	2851±10	7.36±0.2	34±2
CM-HT	14.85±0.6	0.54±0.00	0.62±0.01	2782±6	2.84±0.02	450±21
0^0 AB	15.81±0.4	3.09±0.3	0.76±0.01	3626±21	6.14±0.7	2.4±0.6
0^o HT	15.85±0.2	3.74±0.5	0.69±0.01	3010±11	4.97±0.3	450±203
45^o AB	15.00±0.5	3.14±0.3	0.65±0.00	3207±17	8.36±0.8	1.5±0.3
45^o HT	15.05±0.8	1.12±0.2	0.64±0.00	2360±12	2.63±0.1	550±213
90^o AB	16.24±0.2	3.76±0.8	0.67±0.01	2715±11	7.61±0.6	680±29
90^o HT	17.59±0.6	3.39±0.6	0.68±0.00	2518±8	5.16±0.2	320±18

6.2.4 Chemical composition of corroded surfaces

6.2.4.1 XPS analysis

The XPS was performed on AB and HT corroded samples because the purpose was to examine the type of oxide formation and their analysis in AB and HT corroded samples. Maraging steel powder was processed in a controlled inert atmosphere (Ar) and optimum oxygen level (1000 ppm) in the build chamber, with the result, a thin oxide layer may be formed on the surface of AB samples before corrosion. X-ray photoelectron spectroscopy (XPS) was not conducted on the surfaces of the samples prior to corrosion. It is challenging to distinguish between the formation of oxides in the AB samples before and after corrosion. However, it is evident that the quantity of oxide formed after corrosion will be significantly greater than the amount present before corrosion. Fig. 6.12, depicts the survey spectrum of AB and HT corroded samples, which reflects the nominal composition of the maraging steel.

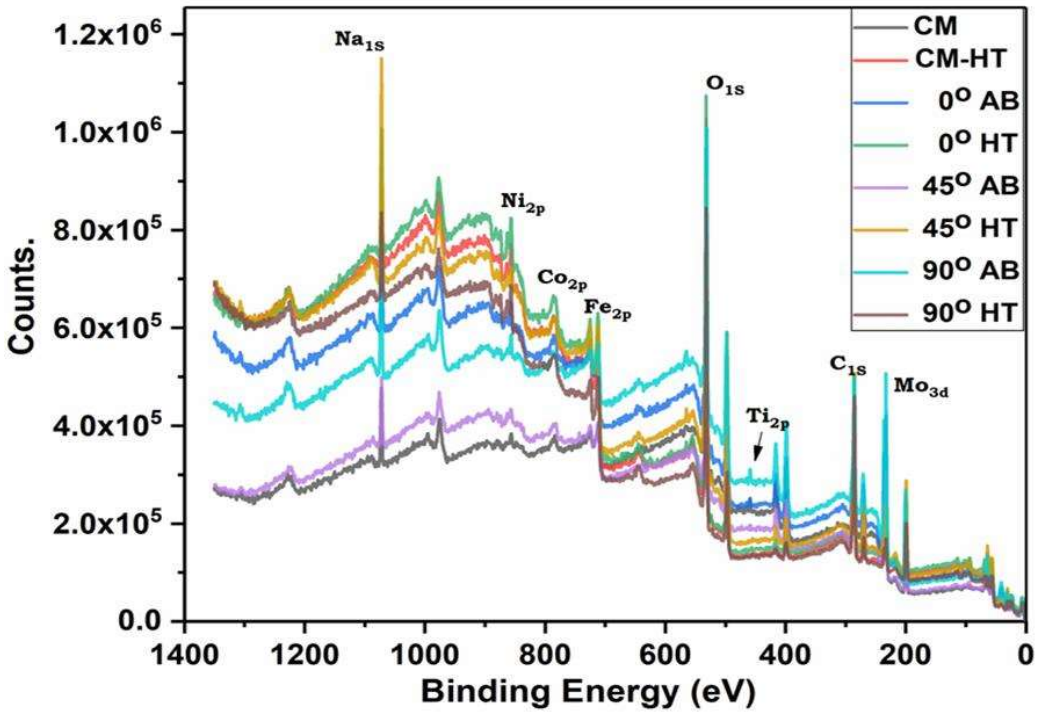

Fig. 6.12. XPS survey of maraging steel in different conditions, showing the presence of Fe, O, Ni, Mo, Ti, Co elements in the corrosion product.

As indicated in Table 6.3, the elemental concentration derived from this spectrum suggests the formation of Fe, Mo, Co, Ni, and Ti oxides or hydroxides on the surface. It is clear from Fig. 6.12, that all the HT results shifted upside after the solution and aging treatment (HT), and the corrosion reaction rate increased, resulting in greater oxide formation on the HT-corroded samples, which displayed higher intensity counts in XPS survey spectra, in line with the literature [168].

Table. 6.3 Chemical composition of the passive film formed on maraging steel in different conditions, in aqueous solution of 3.5% NaCl, as determined from the XPS survey spectra.

Samples	Corrosion Product/Chemical Elements/State on Surface (at%)						
	O_{1s}	Fe_{2p}	Co_{2p}	Mo_{3d}	Ni_{2p}	Ti_{2p}	C_{1s}
CM	32.41	3.94	1.12	6.31	0.93	1.71	41.05
CM-HT	34.73	5.11	1.67	0.51	1.24	0.6	40.85
0° AB	34.82	5.4	1.91	3.91	1.9	0.25	43.67
0° HT	36.21	6.41	2.06	0.97	3	0.03	39.2
45° AB	31.58	5.86	1.6	4.14	1.14	0.34	47.44
45° HT	34.28	6.59	1.3	1.28	1.06	0.09	40.36
90° AB	31.23	4.6	1.5	5.44	0.97	0.61	38.98
90° HT	32.95	5.57	1.58	0.95	2.87	0.26	44.36

The XPS spectra were analysed by deconvolution of peaks in the Fe_{2p}, Mo_{3d}, Ti_{2p}, Co_{2p}, Ni_{2p} and O_{1s} regions for AB/CM and HT samples conditions shown in Figs. 6.13 to 6.17. The typical acquired O_{1s} XPS spectra for 90° AB samples are given in Fig. 6.13(a). The spectra obtained exhibit peaks at 530.5±0.2 eV and 531.5±0.2 eV which are connected to O^{2-} and OH^{-}, chemically attaching to metal ions. Similarly, for AB/CM and HT conditions for all the samples, the peaks were found at 530.2±0.2 eV and 531.3±0.2 eV with increase in intensity. As the HT samples underwent more corrosion, the intensity of hydroxide and oxide peaks increased as compared to AB and CM samples. Satellite peaks in XPS (Xray photoelectron spectroscopy) are additional peaks that appear in the XPS spectrum at higher binding energies in addition to the main core-level peaks. Presence of satellite peaks can indicate the presence of multiple oxidation states of an element.

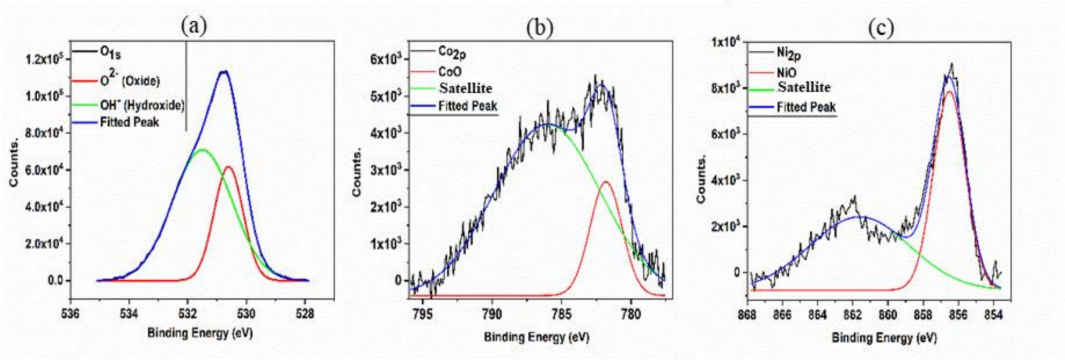

Fig. 6.13 XPS peak spectra in 90° AB condition showing: (a) Oxygen O_{1s} peak spectra (b) Co_{2p} peak spectra (c) Ni_{2p} peak spectra.

Fig. 6.13(b) displays the peak fitting of Co_{2p}. In Co_{2p} spectra, the peaks at 782.2±0.2 eV are ascribed to the binding energies of Co^{2+} producing CoO and the peaks at 786.0±0.2 eV is evident shake-up satellite peak [169]. Fig. 6.13(c) shows the Ni_{2p} XPS spectra produced for the AB/CM and AM-HT maraging steel samples. The peaks positioned at 856.1±0.2 eV was related to Ni_{2p} bonded with O_2, whereas the peaks with a binding energy of 861.5±0.2 is a satellite peak [170].

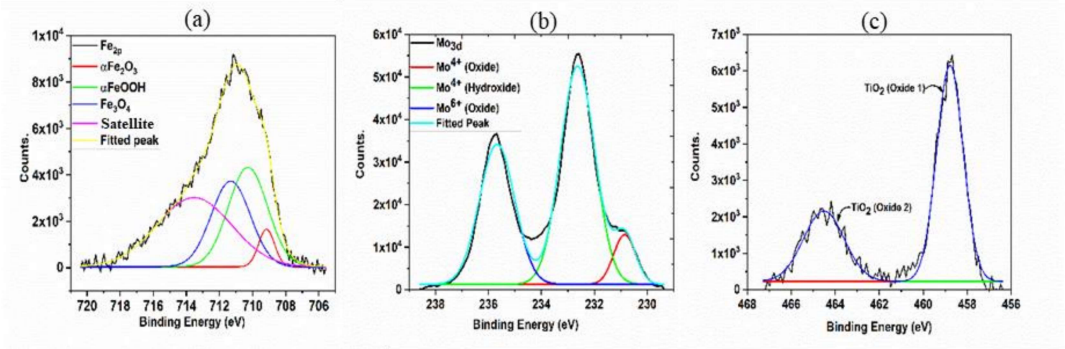

Fig. 6.14 XPS peak deconvolution in CM samples: (a) Fe_{2p} peak spectra fitting showing iron hydroxide and oxide as a corrosion product (b) Mo_{3d} peak spectra fitting (c) Ti_{2p} XPS peak spectra.

The typical Fe_{2p} XPS spectra obtained for the corrosion products are depicted in Figs. 6.14-6.17(a). The peaks positioned at 709.3±0.2 eV, at 710.2±0.2 eV and at 711.4±0.2 eV is connected to the Fe^{2+}, Fe^{3+} (oxide), and Fe^{3+} (Hydroxide) correspondingly. The

satellite peaks are located at 714.4±0.2 eV. The Mo_{3d} XPS spectra obtained for the corrosion products of AB/CM and HT samples are depicted in Figs. 6.16-6.17(b).

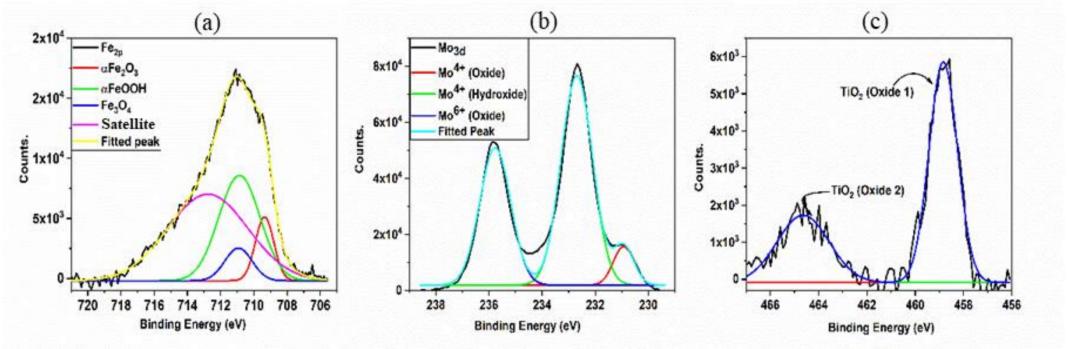

Fig. 6.15 XPS peak fitting of 90°AB condition: (a) Fe_{2p} peak spectra fitting (b) Mo_{3d} spectra fitting (c) Ti_{2p} XPS peak spectra fitting.

CM/AB samples exhibited three peaks at 231.3±0.2 eV, 232.2±0.2 eV, and 235.5±0.2 eV, which correspond to Mo^{4+} (Oxide), Mo^{4+} (Hydroxide), and Mo^{6+} (Oxide) establishing chemical bonds with O^{2-} and OH^{-}, whereas HT samples displayed just two peaks, namely Mo^{4+}(Hydroxide) and Mo^{6+}(Oxide). Figs. 6.16 and 6.17(b) demonstrate that following HT, the intensity of deconvoluted peaks decreased and the Mo^{4+} (Oxide) peak disappeared from spectra.

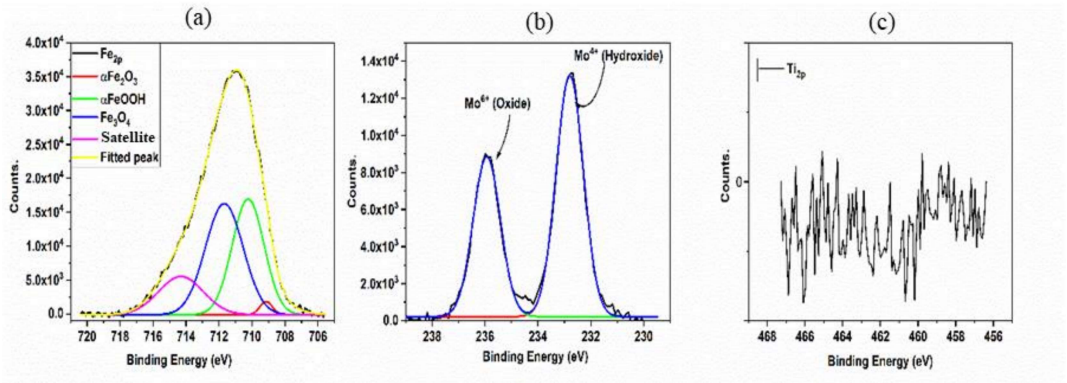

Fig. 6.16 XPS peak fitting in CM-HT condition: (a) Fe_{2p} peak spectra (b) Mo_{3d} spectra fitting and (c) Ti_{2p} XPS peak spectra with negligible intensity.

Lastly, the Ti_{2p} XPS spectra obtained for both CM as well as the AB maraging steel samples in varied orientations of 0°, 45° & 90°, were comparable, as shown in Figs. 6.14 and 6.15(c), and the Ti_{2p} spectra disappeared after HT as shown in Figs. 6.16, 6.17(c).

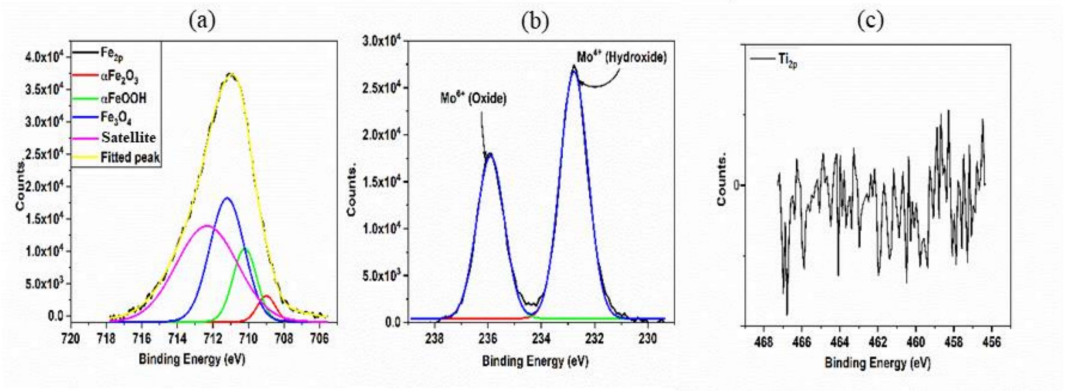

Fig. 6.17 XPS peak spectra fitting of 45° HT sample for (a) Fe_{2p} peak (b) Mo_{3d} spectra (c) Ti_{2p} peak fitting which showed negligible intensity count.

This spectrum displays two well-defined peaks at 458.4±0.2 and 464.1±0.2 eV that is associated with the presence of TiO_2 [171], suggesting that this oxide was present in AB/CM maraging steel corrosion products prior to HT treatments. All the above XPS peak fitting parameters and the nature of the corrosion product formed are summarized in Table. 6.4.

Table 6.4. XPS peak fitting parameters were obtained for the reconstruction of spectra.

S. No.	Core Level	State	Assignment	Binding Energy (eV)
1.	Fe_{2p}	αFe_2O_3 $\alpha FeOOH$ Fe_3O_4 Satellite	Oxide Hydroxide Oxide	709.3±0.2 710.2±0.2 711.4±0.2 714.4±0.2
2.	Mo_{3d}	Mo^{4+} Mo^{4+} Mo^{6+}	Oxide Hydroxide Oxide	231.3±0.2 232.5±0.2 235.5±0.2
3.	Ti_{2p}	TiO_2 TiO_2	Oxide 1 Oxide 2	458.4±0.2 464.1±0.2
4.	Co_{2p}	CoO Satellite	Oxide	782.2±0.2 786.0±0.2
5	Ni_{2p}	NiO Satellite	Oxide	856.1±0.2 861.5±0.2
6.	O_{1s}	O^{2-} OH^-	Oxide Hydroxide	530.2±0.2 531.3±0.2

6.2.4.2 SEM-EDS analysis

To examine the corrosion mechanism, FE-SEM micrographs were taken to differentiate the corrosion behaviour of conventional CM, AB and HT specimens printed in different orientations; horizontally, diagonally, and vertically (0^o, 45^o and 90^o). Fig. 6.18(a) depicts the formation of a non-protective corrosion layer that covers the whole surface of the CM sample (visual observation). Further analysis at higher magnification in Fig. 6.18(b) reveals the development of oxide with the rupture of the passive film, which facilitated electrolyte penetration through the film. The area scan EDS analysis of Fig. 6.18(b) reveals the elements responsible for the formation of corrosion products, namely Fe, Ti, Mo, Co, Na, and Cl compounds as depicted in Fig. 6.18(c), similar to that indicated in the XPS spectra analysis.

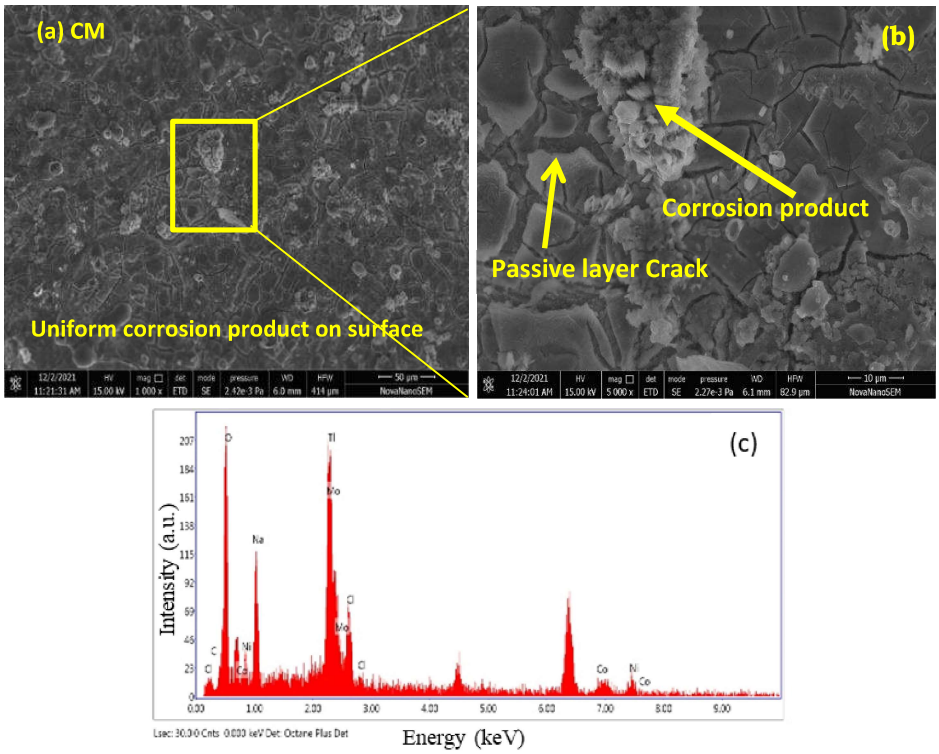

Fig. 6.18. Corrosion surface morphology on CM specimen showing (a) uniform corrosion product on the surface (b) magnified view of corrosion product and passive layers with cracks and (c) EDS area scan of corrosion product.

Likewise, Figs. 6.19(a) and 6.20(a), show the non-uniform passive film with interconnected cracks for 0° AB and HT corroded samples. Figs. 6.19(b) and 6.20(b) shows magnified views of the corrosion products with passive film. The EDS scan depicted in Fig. 6.19(c) reveals Fe, Ti, Mo, Co, and Ni compounds under AB conditions. However, after HT, the EDS scan reveals primarily Fe, Co, and Ni, while precipitate-forming elements such as Ti and Mo are reduced as revealed in Fig. 6.20(c). The observed results are in line with the XPS results depicted in Fig. 6.12.

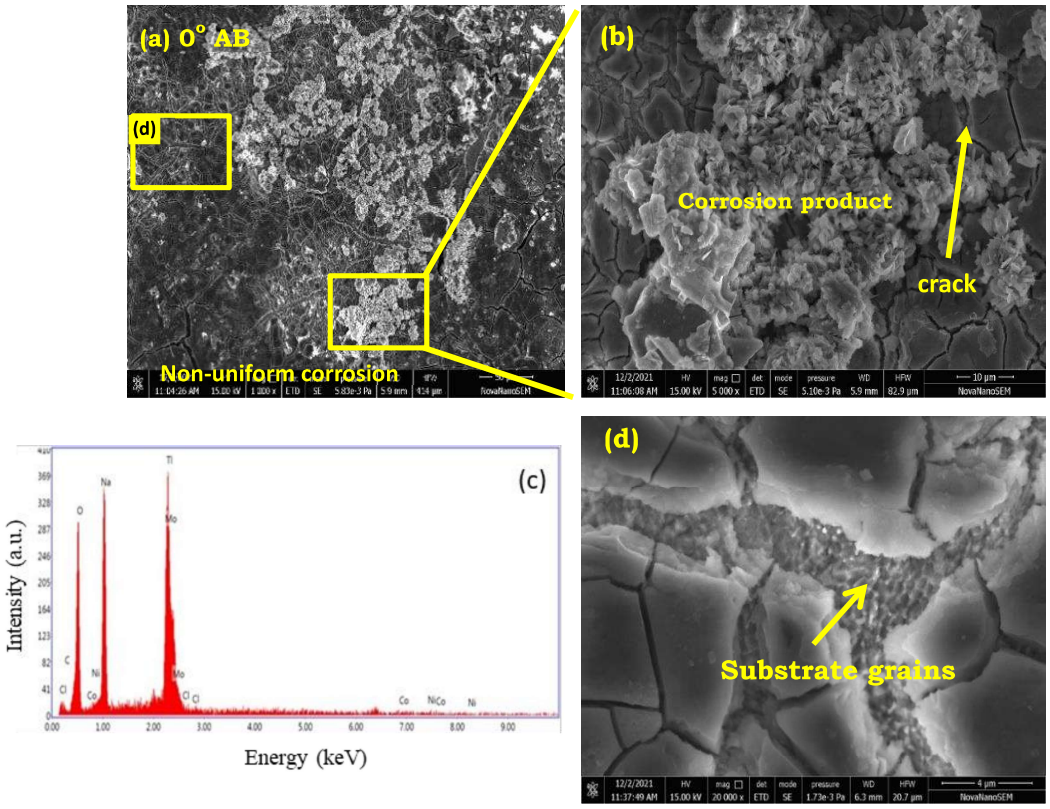

Fig. 6.19. Corrosion surface morphology of 0° AB specimen showing (a) non uniform corrosion product on surface (b) magnified view of corrosion product (c) EDS area scan of corrosion product and (d) microstructural morphology of AB sample through passive layer.

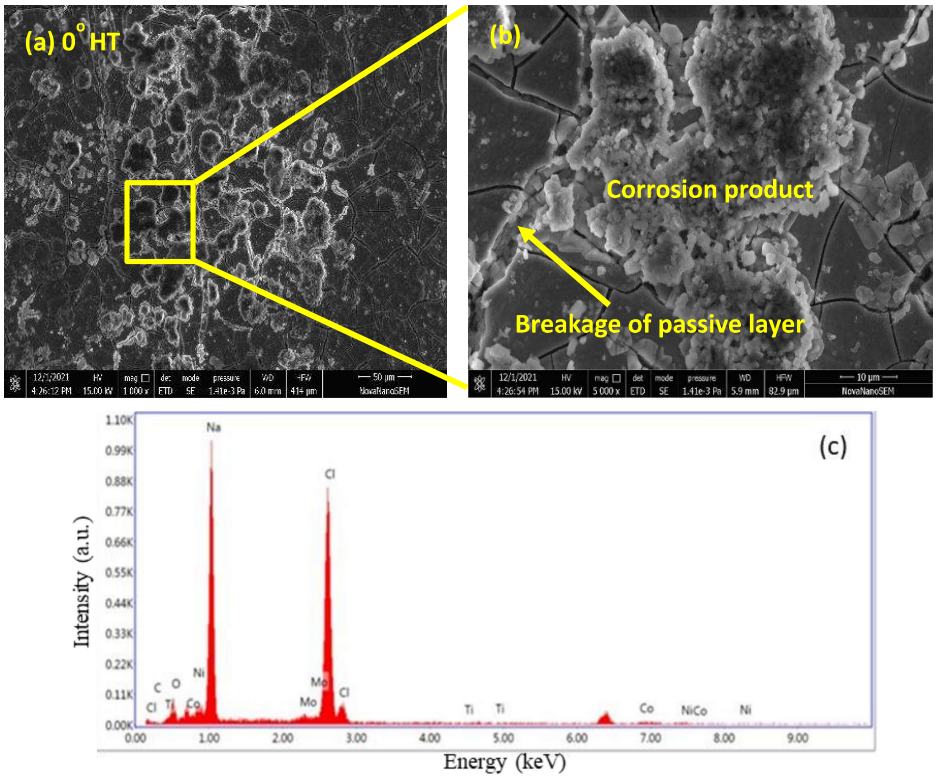

Fig. 6.20. Corrosion surface morphology of 0° HT specimen showing: (a) non-uniform corrosion product on surface (b) magnified view of corrosion product and passive layer film crack (c) EDS scan of corrosion product.

In addition, the side view of a sample is polished, etched and examined using SEM for a comprehensive corrosion investigation and to determine the effect of layer orientation on corrosion. Fig. 6.21(a) is a side view of a CM sample displaying the lowest observed corrosion layer thickness, with minimal pitting, indicating uniform surface corrosion. Fig. 6.21(b) depicts a thick corrosion layer with interlayer-directed pitting. Similarly, the thickest corrosive layer among AB additive samples occurred in the 90° AB samples, and deep pits were found from the corrosion surface to the metal matrix through the interlayer region as shown in Fig. 6.21(c).

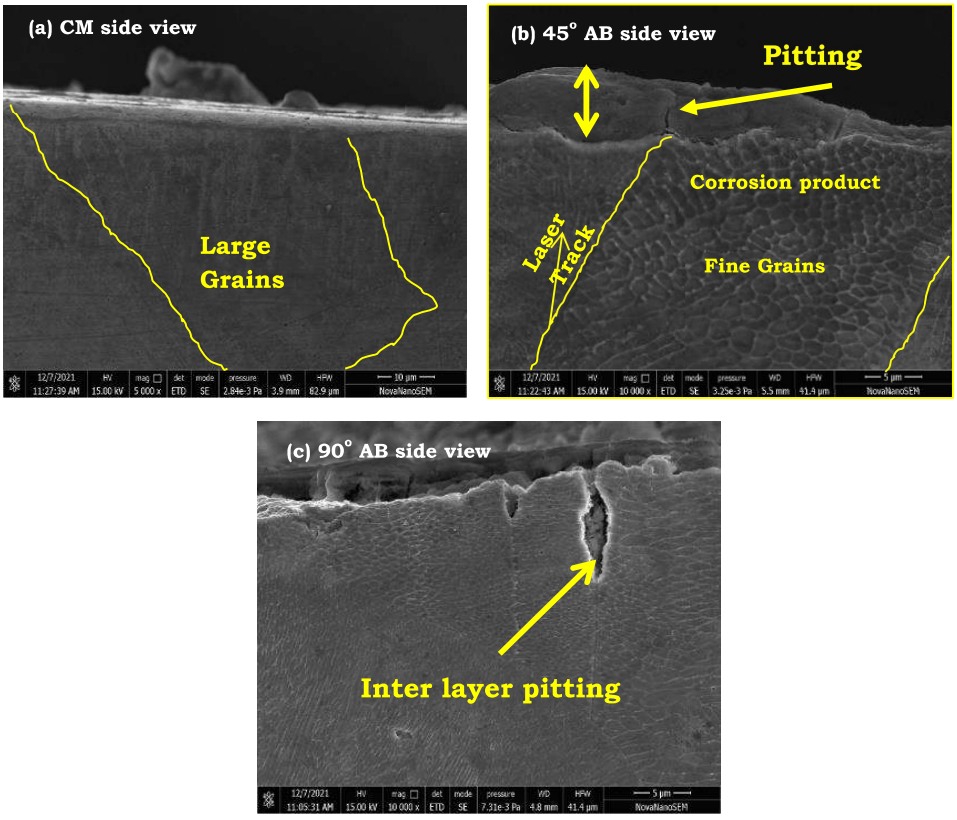

Fig. 6.21 Side surface morphology of corroded specimens in different conditions showing: (a) very thin corroded film in CM samples (b) pitting along layer junction in 45° AB and (c) inter layer pitting corrosion in 90° AB.

Fig. 6.22 depicts the side view of the HT sample for conventional and additive 45° and 90° orientations. Fig. 6.22(a) depicts conventional HT sample with a shallow corrosion layer and blunt pitting characteristics. In Fig. 6.22(b), in the 45° HT sample, localized corrosion was found and subsurface pitting was also visible. The side corrosion morphology of the 90° HT sample is depicted in Fig. 6.22(c), where the corrosion-affected region and martensite matrix are clearly visible.

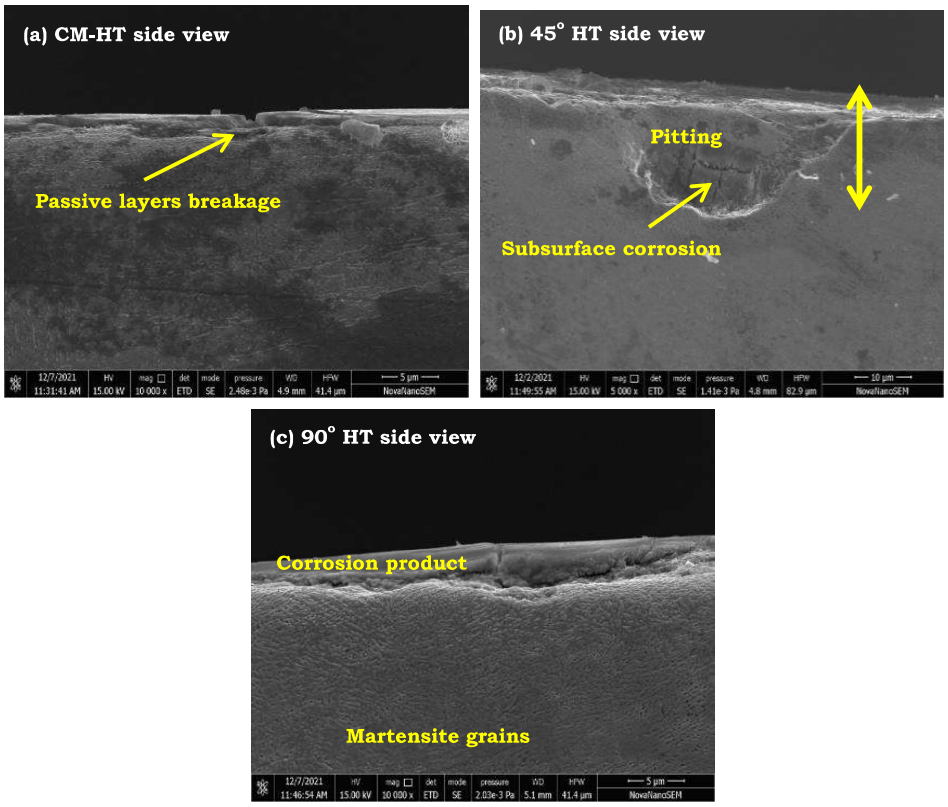

Fig. 6.22 Side surface morphology of corroded specimen in different conditions: (a) CM-HT. (b) 45o HT and (c) 90o HT specimen.

6.2.5 Corrosion Mechanism

The oxidation and reduction reactions occur simultaneously when maraging steel is exposed to a 3.5% NaCl solution in water. In AB and AM-HT sample conditions, the solution reacts with the exposed surface where heterogeneity in chemical composition, surface energy, interlayer region and precipitates are present. The mechanism of pit formation in the AB sample has been demonstrated. The Fe present in the interlayer region corrodes in a series of reactions as detailed below.

Stage I

$Fe = Fe^{2+} + 2e^{-}$ at anode

$O_2+2H_2O+ 4e^{-} = 4OH^{-}$ at cathode

Stage II

$Fe^{2+} + 2OH^- = Fe(OH)_2$

After the preceding two steps, the subsequent reaction (Fig. 6.23) causes a layer of iron hydroxide to form on the cathode surface close to the pitting area.

$4Fe(OH)_2 + O_2 + 2H_2O \rightarrow 4\ Fe(OH)_3$ (Deposited hydroxide layer)

It also can be written in oxide form as:

$Fe(OH)_3 \rightarrow Fe_2O_3 \cdot xH_2O$

The chloride ions present in the solution attack the iron surface at the anode aggressively, resulting in the dissolution of iron through pitting [172]

$Fe + Cl^- = Fe\ (Cl^-)_{metal\ surface}$

$Fe(OH) + FeCl = Fe + FeOH^+ + 2e^-$ at anode

$FeOH^+ + H^+ = Fe^{2+}_{(solution)} + H_2O$

$Fe + 2Cl_{(sol.)} = FeCl_2 + 2e^-$

The production of iron chloride above the corrosion product increases the dissolution of iron by attacking its surface.

There is no reaction possible between Mo and water; instead, Mo combines with O_2 to generate oxide as per the reaction below.

$2Mo + 3O_2 = 2MoO_3$

Which is not a protective scale in the presence of NaCl, and dissolves further due to the Cl attack [173].

$2Mo + 5Cl_2 \rightarrow 2MoCl_5$ (black)

The Titanium reacts with oxygen as follows i.e.

$Ti + O_2 = TiO_2$

In the presence of NaCl, a series of chemical reactions prevent the formation of a protective TiO_2 scale, which is the primary cause of the destruction of passive layers in AB samples. Initial TiO_2 reactions with NaCl and O_2 degrade the protective scale in the following manner [174]:

$5TiO_2 + 4NaCl + O_2 \rightarrow Na_4Ti_5O_{12} + 2Cl_2$

Other chemical reactions implicated in the present study's mechanisms are of little relevance. Pitting is visible in the interlayer region at two sites in the diagram, and the region adjoining it acts as a cathode, as depicted in the schematic diagram of the mechanism. On substrate, fine cellular and columnar grains can also be observed as shown in Fig. 6.23.

The corrosion mechanism of HT sample can be portrayed in a similar manner as described above only the Ti constituents would not participate in the corrosion reaction because after aging Ti present in the matrix, participate in precipitate formation. Schematically, the corrosion mechanism of HT samples is represented in Fig. 6.24, which reveals deep wide pitting characteristics.

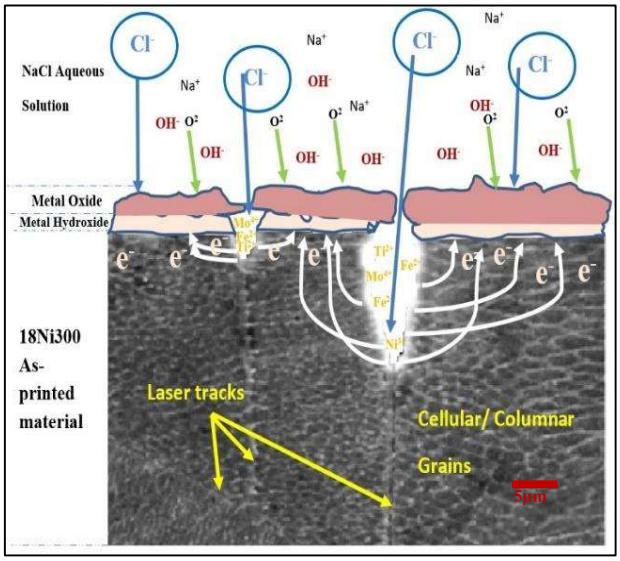

Fig. 6.23. Mechanism of corrosion in the present maraging steel in as-built (AB) condition.

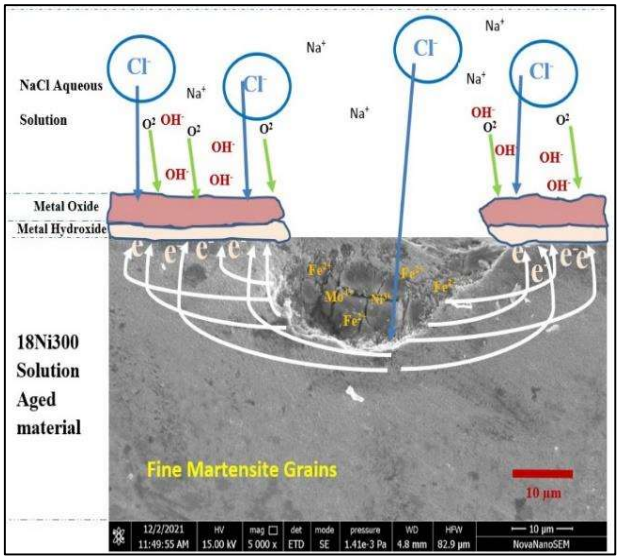

Fig. 6.24 Mechanism of corrosion in the present maraging steel in as-built (AB) and heat treated (HT) condition.

6.3 DISCUSSION

6.3.1 Microstructural Characterization and Phase analysis

As-built (AB) specimen, shows process characteristics i.e., laser tracks, scan pattern, melt pool and layer thickness, in meso-structure. Because of the high cooling rate (10^5 – 10^7 K/s) and uneven heating/cooling situation during PBF-LB, two types of microstructures can be seen in the AB samples. The visible larger sub-structure has a slower cooling rate than the smaller sub-structures. It is worth mentioning that there are two substructures in Figs. 6.3(a), 6.4(a) and 6.5(a) that appear to be cellular and columnar-shaped, respectively. The differences in shape are due to the orientation and the difference in mesostructure is governed by process parameters [175]. In Figs. 6.3(b) 6.4(b) and 6.5(b), the lath martensite structure can be observed. In the HT sample conditions, the corrosion is mainly governed by the precipitate and the percentage of reverted austenite formed in the sample [176].

6.3.2 Corrosion Behaviour of AB and As received Conventionally Manufactured (CM) specimens

From the Table. 6.1, 0^o AB samples showed the lowest OCP value i.e. -0.36±0.05 V among AB samples. and it can be also noted that the OCP of AM-HT samples is around the same for all orientations i.e. ~(-0.37 V), This indicates that the onset of corrosion in the CM/AB sample is more delayed than in HT samples [177]. In the present investigation from Fig. 6.6(a), it was found that as-built orientations affect the corrosion rate, these results are concurrent with the residual stress and exposure angle of layers to the corrosive media. In 90^o AB samples, interlayer regions are more exposed to corrosive media and interlayer regions are more susceptible to corrosion due to which the passive layer formed on the surface is easily broken and further pitting starts. Interlayer corrosion was also observed in 45^o AB samples but lower than 90^o AB samples, due to a less

effective area of exposure to the corrosive media. Related results were observed in other investigations but in different materials [178]. The residual stress decreases the surface atomic density and activation energy, therefore, decreases the corrosion resistance of additively manufactured AB samples.

The parameters of the fitted impedance spectra of anodic dissolution of maraging steel are presented in Table. 6.2, and it can be observed from Eqs. (2.9, 2.10) that the intermediate resistance R_3 shows very less effect on the total impedance value. Only the variation of R_1 and R_2 gives maximum variation in impedance (Z) observed as per Eq. (2.9). From the results, it is clear that as the built orientation increased the charge transfer resistance decreased with the results of the impedance (Z) value decreased as per the above equation, and the corrosion rate increased. Figs. 6.9(a) and 6.10(a) illustrate the Bode magnitude graphs. The frequency-independent zone, which represents pure solution resistance, can be detected at higher frequencies, while the mid-frequency region is dominated by capacitance and the low-frequency region is ruled by solution R_1 + charge transfer resistance R_2. The Bode phase angle versus frequency plot Figs. 6.9(b) and 6.10 (b) reveal two humps, one of which is huge and the other is blunt. For all maraging steel samples, the phase angles associated with maximum vary within a narrow range (65-70). From the results, it is clear that all maraging steels have a phase angle drop to zero degrees at higher frequencies, showing that solution resistance dominates impedance at these frequencies. Further, the phase angle drop can also be detected in the low-frequency zone, demonstrating that polarization resistance dominates the impedance.

6.3.3 Corrosion Behaviour of AM-HT and CM-HT specimens

From potentiodynamic polarization Fig. 6.6(b) it is clear that all graphs in the HT condition shifted rightwards on the current density axis and downwards on the potential

axis. This implies the HT sample is more prone to corrosion than in CM/AB conditions. Since the solution ageing treatment (HT) led to the formation of the reversed austenitic and intermetallic precipitates in the present study [179], the negative increase in E_o value indicates a more activated condition for corrosion, observed for the HT samples, was due to the presence of more heterogeneities in the grain, which resulted in the breaking of the film formed on the surface of the aged sample. Fig. 6.6(b) shows that the 45^o HT samples showed max. current density and minimum corrosive potential which confirm the corrosion rate dominant by reverted austenite in HT samples similar observation was reported in the literature [180, 181]. The Nyquist and Bode plots in Figs. 6.8 and 6.10 support the result obtained from the polarization graph. As illustrated in Fig. 6.8, impedance spectra were produced in the form of Nyquist plots from solution and aged additive and conventional samples. At high frequencies, the Nyquist diagrams consisted of a depressed capacitive semicircle followed by a well-defined inductive loop at low frequencies. In this study, the 45^o HT samples with the highest reversed austenite had the smallest arc diameter compared to other HT samples. Fig. 6.10 displays the EIS results for HT samples as Bode graphs. The Bode plot provides a more precise representation of the frequency-dependent electrochemical behaviour than the Nyquist plot, in which the frequency values are implicit. In reality, the Bode plot is a superior alternative to the Nyquist plot due to its ability to eliminate any errors in fitting the Nyquist semicircle and the longer measurement periods associated with low frequency [182].

6.3.4 Chemical composition and surface morphology of corroded specimens

In Fig. 6.12, the XPS survey spectra show Na, Cl, O, C, Fe, Co, Mo, Ti, Ni, peaks for AB additive manufactured, CM, HT additive and conventional samples. It can be clearly observed from Table. 6.3 that after HT, due to the formation of intermetallic precipitate the precipitate-forming constituents get reduced, with the results Ti, Ni, Mo, Co intensity

in the XPS survey get reduced. The O_{1s} spectra suggest the oxide and hydroxide peaks which help in the other spectra analysis as shown in Fig. 6.13(a). Ni_{2p} and Co_{2p} spectra are similar for all conditions and only a less percentage of oxides is observed in the corrosion products represented in Figs 6.13 (b) and (c). This can also be observed in individual spectra of components as there were no Ti compounds formed in the HT corroded samples similarly in Mo spectra, individual peaks get reduced in the comparison to CM/AB spectra depict in Figs. 6.14, 6.15(b, c), 6.16 and 6.17(b, c). The chemical composition formed on the surface of the corroded sample is calculated in atomic percentages, as represented in Table. 6.3, support the above-mentioned discussion. Based on the results obtained for Fe_{2p} spectra fitting, in this work, an oxide development model can be presented as follows. Initially, upon initiation of corrosion, the oxide coating comprises iron oxide of Fe_2O_3 and a thin film of FeOOH on the top. With the increased O_2 exposure, Fe_3O_4 and FeOOH continue to grow until the oxide growth saturates, observed in literature [183-185]. The Ti peaks get suppressed in HT samples due to the formation of Ni_3Ti precipitation in aged samples, by virtue of this TiO_2 could not be detected in the corrosion product of HT samples as depicted in Figs. 6.16 (c) and 6.17 (c).

The SEM analysis of unaged samples in Figs. 6.18, 6.19 and aging treated samples in Fig. 6.20 exhibited pitting and corrosion by-products. Note that deeper rusting was observed in HT samples. In Fig. 6.19(a), a magnified view is given. Fig. 6.19(d) shows a contrast between the base metal and the metal affected by corrosion. The difference, in contrast, is caused by exposure to the underlying microstructure. The existence of precipitates and austenite phases in HT samples was found to increase their sensitivity to corrosion. Due to the existence of an almost single-phase, corrosion susceptibility was similar in as-built samples. In the as-built and as-received conventional (CM) samples, the EDS area scan

from Figs. 6.18(c) and 6.19(c), it is clear that there are peaks of Ti, Mo, and corrosion-resistant oxide layer but after aging treatment, these peaks are getting suppressed, Fig. 6.20(c) and thus preventing the formation of resistive oxides layer, so it is easy to break passive layers, with the result, deeper pits and subsurface pit was formed in HT samples as shown in 6.22(b).

6.4 CHAPTER SUMMARY

Major inferences drawn from the corrosion study are mentioned below.

1. The corrosion behaviour of PBF-LB maraging steel was governed by processing factors such as layer orientation and microstructural inhomogeneity.

2. The corrosion rates of AB samples were found to increase as the built orientation increased and AB samples showed better corrosion resistance than as-received conventional (CM) samples.

3. Aging caused deterioration in corrosion resistance in PBF-LB maraging steel and also in conventional maraging steel. The corrosion behaviour of the aged maraging steel produced by PBF-LB was influenced by the precipitation and reverted austenite present. The best corrosion resistance was observed in 0^{o} orientation among all the orientations.

4. Pitting corrosion was observed in both as-built (AB) and heat treated (HT) specimens. Pitting started from the interlayer region of AB samples and grows towards the interlayer region while homogenous deep blunt pitting was observed with subsurface corrosion in HT samples.